Accepted Manuscript

Shape adaptive RBF-FD Implicit Scheme for Incompressible Viscous Navier-Strokes Equations

A. Javed, K. Djijdeli, J.T. Xing

PII: S0045-7930(13)00411-8
DOI: http://dx.doi.org/10.1016/j.compfluid.2013.10.028
Reference: CAF 2340

To appear in: *Computers & Fluids*

Received Date: 4 April 2013
Revised Date: 12 September 2013
Accepted Date: 22 October 2013

Please cite this article as: Javed, A., Djijdeli, K., Xing, J.T., Shape adaptive RBF-FD Implicit Scheme for Incompressible Viscous Navier-Strokes Equations, *Computers & Fluids* (2013), doi: http://dx.doi.org/10.1016/j.compfluid.2013.10.028

Shape adaptive RBF-FD Implicit Scheme for Incompressible Viscous Navier-Strokes Equations

A. Javed*, K. Djijdeli, J. T. Xing

Abstract

Meshless methods for solving fluid flow problems have become a promising alternative to mesh-based methods. In this paper, a meshless method based on radial basis functions in a finite difference mode (RBF-FD) has been developed for the incompressible Navier-Stokes (N-S) equations in primitive variable form. Pressure-velocity decoupling has been achieved using a fractional step method whereas time splitting has been done using both explicit and implicit schemes. The RBF-FD implicit scheme shows better accuracy and stability, and is able to accurately capture higher gradients of field variables even at coarser grids; unlike the RBF-FD explicit scheme where loss of accuracy was especially prominent at places with larger gradients. To overcome the ill-conditioning and accuracy problems arising from the use of non-uniform and random node distribution, a novel concept of adaptive shape parameter (ASP) for RBF functions is introduced. The use of ASP allows much finer nodal distribution at regions of interest enabling accurate capturing of gradients and leading to better results. The performance of the

*Corresponding Author

Email addresses: `A.Javed@soton.ac.uk` (A. Javed), `kkd@soton.ac.uk` (K. Djijdeli), `jtxing@soton.ac.uk` (J. T. Xing)

implicit RBF-FD scheme with the ASP strategy is validated against a variety of benchmark problems, including lid driven cavity flow problems, and steady and unsteady laminar flow around circular cylinder at various Reynolds, and is found to be in good agreement with the existing results.

Keywords: Meshless method, Radial Basis Function in Finite Difference Mode, explicit/implicit time discretization of N-S equations, Adaptive Shape Parameter, CFD, Incompressible Navier Strokes equations

1. Introduction

In the past two decades, meshless methods have emerged as a class of effective numerical techniques for the solution of various engineering problems. The aim of these methods is to eliminate, at least, the structure of the mesh and approximate the solution entirely using a set of arbitrarily distributed nodes (or particles). They have the capability to accommodate larger deformations as well as coping with the domains comprising of irregular/complex geometries with relative ease. Moreover, it is easier to add or remove nodes from the domain during the analysis which otherwise is a tedious task in case of mesh-based methods. Some of the well-known meshless methods are smooth Particle hydrodynamic (SPH) method [1], diffuse element method (DEM) [2], element free Galerkin method (EFGM) [3], reproducing Kernel particle method (RKPM) [4], partition of unity method (PUM) [5], finite point method (FPM) [6], and Local Petrov Galerkin Method (LPGM) [7].

In recent years, the class of meshless methods, based on Radial Basis Functions (RBFs), have become attractive for solving PDEs [8], [9], [10], [11], [12], [13], [14], [15], [16], [17]. Initially, RBFs were developed for multivariable data and function interpolation, especially for higher dimension problems. The advantages of using RBFs as a truly meshless method have been verified by its mesh independence, superior convergence and adaptivity to high dimension. On the other hand, it is well known that the coefficient matrices for RBF collocation methods becomes ill- conditioned when the number of nodes increases. Various researchers have suggested use of local RBF methods to cope with ill-conditioning problem [8], [9], [10]. These local RBF methods compromise on spectral accuracy and come up with a sparse, well-conditioned linear system which is also more flexible in handling non-linearity. Among these, RBF-FD has been independently proposed by Tolstykh et al. [10] and Wright et al. [8] for different types of applications. The technique provides a better conditioned and sparse linear system with greater flexibility to handle non-linearity. The idea is to generalize the use of finite difference on a domain containing arbitrary / random nodes instead of a regular grid.

Selection of appropriate shape parameter of RBF function is extremely important to ensure accuracy while solving equations using RBF method. Various authors have investigated the optimal values of shape parameter for RBFs. Franke [11] investigated 30 different interpolation schemes and suggested an mathematical relationship for optimal value of shape parameter for multiquadratic RBFs. Hardy [12] suggested a value of optimal shape parameter based on average distance of the neighbouring nodes within the influence domain from point of interest. Rippa [13] recommended an algorithm for selecting a good value of shape parameter in RBF interpolation. The fact is that the accuracy of results is greatly influenced by the value of shape parameter and the choice of an optimal value of shape parameter is still open to further research.

RBF-FD technique provides a good potential of solving fluid dynamics problems (like Navier- Strokes Equations) due to their ability to handle dense grids. Chinchapatnam et al. [14] provided the method for solving incompressible Navier Strokes equation in vorticity streamfunction formulation using RBF-FD method. Vorticity streamfunction formulation of N-S equations however, cannot be extended to 3-D problems and is limited to incompressible regime only. Moreover, physical parameters (velocity and pressure) cannot be calculated directly using this formulation. It is therefore logical to investigate the application of RBF-FD approach for N-S equations in their primitive variable form.

A method of solution of Navier-Strokes equations in their primitive variable form is therefore presented using RBF-FD technique. Pressure-Velocity decoupling, in N-S equations, has been achieved by fractional step method based on Chorin algorithm. Time discretization of resultant momentum equation after decoupling the pressure term has been achieved using explicit and implicit approaches. Explicit RBF-FD employs Euler explicit method for temporal discretization of momentum equations. For implicit approach, second order implicit Crank-Nicolson method has been used for viscous term whereas convective term is discretized using second order accurate Adams-Bashforth scheme. Suggested meshless schemes are tested for uniform, non-uniform and random particle distributions and have been validated by the benchmark solutions of lid driven cavity flow problems provided by Ghia et al. [18]. Excellent numerical results are obtained on non-uniform node distribution using the implicit RBF-FD method. Accuracy tests of Implicit RBF-FD scheme have been performed. Moreover, Implicit RBF-FD scheme has also been used to simulate steady and unsteady laminar flow around circular cylinder at different Reynolds numbers.

In addition, the authors have also investigated the novel concept of using adaptive shape parameters, for Radial Basis Function, within the domain instead of globally similar values as used conventionally. The aim is to maintain the well conditioning of coefficient matrix for RBF-FD weights in a domain represented by non-uniform nodal distribution. The values of shape parameters have been selected to keep the condition number of coefficient matrix to low which ultimately affects the accuracy of the interpolation.

This paper is organised as follows: Section 2 presents the governing Navier-Stokes equations in primitive variables along with space and time splitting. A basic idea of the RBF-FD collocation method is also presented. Section 3 outlines the solution algorithm. A novel concept of using adaptive shape parameters of RBF functions is presented in Section 4. Detail of numerical tests has been presented in Section 5 and finally conclusions are drawn in Section 6.

2. RBF-FD for Incompressible N-S Equations

The time dependant, incompressible and viscous Navier-Strokes equations in non-dimensional primitive (pressure-velocity) variable form are expressed as:

$$\nabla.\vec{V} = 0 \tag{1}$$

$$\partial\vec{V}/\partial t = -\nabla P - \left(\vec{V}.\nabla\right)\vec{V} + (1/Re)\,\nabla^2\vec{V} \tag{2}$$

where $\vec{V}$ is the velocity vector, P is the pressure, and Re is the Reynolds number. One of the major difficulties faced during numerical solution of transient Navier-Strokes equations in primitive variable form is that the continuity equation does not contain a time derivative. In order to address this problem, the constraint of mass conservation is achieved by coupling the pressure term with continuity equation. For this purpose, an intermediate velocity term $\vec{V}^*$ is introduced, between two consecutive time steps, to decouple pressure term from momentum equation. The class of these methods is known as fractional step methods. In this research, the solution scheme uses Chorin algorithm [19]. The method is based on the non-incremental pressure correction which provides simple method of time discretization using fractional step approach. Other solution schemes may also be developed using different time discretization methods [20]. Using this approach, equation (2) can be written as:

$$\frac{\vec{V}^* - \vec{V}^n}{\partial t} = -\left(\vec{V}.\nabla\right)\vec{V} + (1/Re)\,\nabla^2\vec{V} \tag{3}$$

the pressure term in momentum equation can then be linked with velocity as:

$$\frac{\vec{V}^{n+1} - \vec{V}^*}{\partial t} = -\nabla P^{n+1} \tag{4}$$

where $\vec{V}^n$ and $\vec{V}^{n+1}$ are the velocity values at n^{th} and $(n+1)^{th}$ time step respectively and P^{n+1} is the pressure value at $(n+1)^{th}$ time step. Now, from continuity equation (1):

$$\nabla\vec{V}^{n+1} = 0 \tag{5}$$

Substituting the value of $\vec{V}^{n+1}$ from equation (4) into (5) leads to,

$$\nabla^2 P^{n+1} = (1/\Delta t)\nabla.\vec{V}^* \tag{6}$$

Equation (5) is called pressure Poisson equation. By incorporating pressure term into continuity equation, the continuity is satisfied in the process of solution of transient flow problem.

2.1. Space Splitting

RBF-FD scheme is used to approximate the spatial derivatives appearing in equations (3), (4) and (6). RBF-FD is the generalization of classical finite difference method over scattered nodes. The essence of RBF in Finite difference mode is that derivative of any dependant variable can be expressed as weighted linear sum of same variable values at surrounding data points in the support domain. Using classical finite difference approach, the derivative of any parameter u at any node, say x_1, can be expressed as

$$\mathcal{L}\mathbf{u}(x_1) = \sum_{j=1}^{N} \mathbf{W}_{1,j}^{(\mathcal{L})} u(x_j) \tag{7}$$

where N is the number of nodes in the support domain of node x_1, $\mathbf{u}(x_j)$ is the value of parameter $\mathbf{u}$ at node x_j and $\mathbf{W}_{1,j}^{(\mathcal{L})}$ is the weight of corresponding differential operator $\mathcal{L}$ at node x_j for node x_1 as shown in figure 1. The standard RBF interpolation for a set of distinct points $x_j \epsilon \mathbf{R}^d, j = 1, 2, ...N$ is given by:

$$\mathbf{u}(x) \approx s(x) = \sum_{j=1}^{N} \lambda_j \phi(\|x - x_j\|) + \beta \tag{8}$$

where $\phi(\|x - x_j\|)$ is the radial basis function, $\|.\|$ is the standard Euclidean norm and λ_j and β are the expansion coefficient. Some of the common radial basis functions are given in Table 1. In Lagrange form, equation (8) can be written as:

$$\bar{s}(x) = \sum_{j=1}^{N} \mathcal{X}\left(\|x - x_j\|\right) u\left(x_j\right) \tag{9}$$

where $\mathcal{X}\left(\|x - x_j\|\right)$ satisfies the cardinal conditions as

$$\mathcal{X}\left(\|x_k - x_j\|\right) = \begin{cases} 1, & \text{if } k = j \\ 0, & \text{if } k \neq j \end{cases} \qquad k = 1, 2, ...N \tag{10}$$

Applying the differential operator $\mathcal{L}$ on equation (9) at node x_1 yields:

$$\mathcal{L}u\left(x_1\right) \approx \mathcal{L}\bar{s}\left(x_1\right) = \sum_{j=1}^{N} \mathcal{L}\mathcal{X}\left(\|x_1 - x_j\|\right) u\left(x_j\right) \tag{11}$$

Using equations (7) and (11), RBF-FD weights $\mathbf{W}_{1,j}^{(\mathcal{L})}$ are given by

$$\mathbf{W}_{1,j}^{(\mathcal{L})} = \mathcal{L}\mathcal{X}\left(\|x_1 - x_j\|\right) \tag{12}$$

The weights can be computed by solving the following linear system [14]:

$$\begin{bmatrix} \Phi & e \\ e^T & 0 \end{bmatrix} \begin{bmatrix} W \\ \mu \end{bmatrix} = \begin{bmatrix} \mathcal{L}\phi_1 \\ 0 \end{bmatrix} \tag{13}$$

where $\Phi_{i,j} = \phi\left(\|x_j - x_i\|\right), i, j = 1, 2, \ldots, N,\ e_i = 1, 2, \ldots, N,\ \mathcal{L}\phi_1$ represents the column vector $\mathcal{L}\phi_1 = \left[\mathcal{L}\phi\|x - x_1\|\mathcal{L}\phi\|x - x_2\| \ldots \mathcal{L}\phi\|x - x_N\|\right]^T$ evaluated at node x_1 and μ is a scalar parameter which enforces the condition:

$$\sum_{j=1}^{N} \mathbf{W}_{1,j}^{(\mathcal{L})} = 0 \tag{14}$$

Evaluation of equation (13) at each node x_1 gives weights $\mathbf{W}_{1,j}^{\mathcal{L}}$ of all the nodes in the support domain for particular differential operator $\mathcal{L}$. Corresponding weights and location of nodes in support domains are then used to approximate the complete differential equation at node x_1.

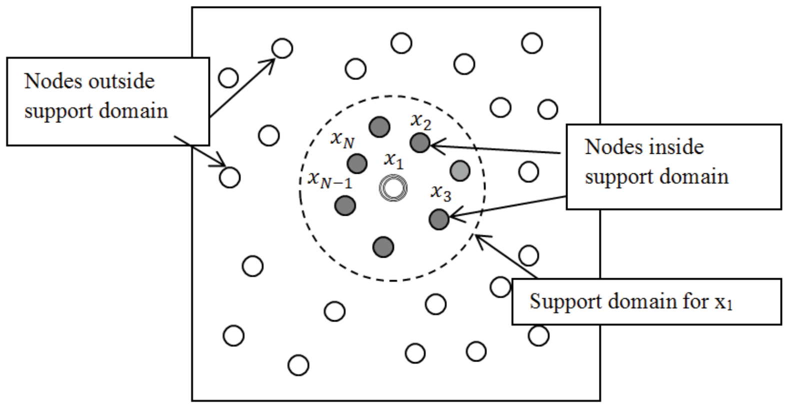

Figure 1: Support domain of a reference node

RBF-FD approximation of spatial derivatives appearing in equations (3), (4) and (6) can be obtained, at any node i, using values of parameters at surrounding nodes within the influence domain and their corresponding RBF-FD weights in equation (7). RBF-FD approximation of spatial derivatives appearing in equations (6) and (4) in 2-D Cartesian component form can be written as:

$$\sum_{j=1}^{N}\left(\mathbf{W}_{i,j}^{(xx)}+\mathbf{W}_{i,j}^{(yy)}\right)P_j^{n+1}=\frac{1}{\Delta t}\left(\sum_{j=1}^{N}\mathbf{W}_{i,j}^{(x)}u_j^{*}+\sum_{j=1}^{N}\mathbf{W}_{i,j}^{(y)}v_j^{*}\right) \tag{15}$$

$$\frac{u_i^{n+1}-u_i^{*}}{\Delta t}=-\sum_{j=1}^{N}\mathbf{W}_{i,j}^{(x)}P_j^{n+1} \tag{16}$$

$$\frac{v_i^{n+1}-v_i^{*}}{\Delta t}=-\sum_{j=1}^{N}\mathbf{W}_{i,j}^{(y)}P_j^{n+1} \tag{17}$$

where, u_i and v_i are the Cartesian components of velocity vector $\vec{V}$ at node i in x and y directions respectively, N is the total number of interior and

Table 1: Commonly used radial basis functions

Type of radial basis function	Expression of $\phi(r)$
Multi-quadratic (MQ)	$\phi(r) = \sqrt{r^2 + \sigma^2}$
Inverse Multi-quadratic (IMQ)	$\phi(r) = 1/\sqrt{r^2 + \sigma^2}$
Inverse Quadratic (IQ)	$\phi(r) = 1/(r^2 + \sigma^2)$
Gaussian (GA)	$\phi(r) = \exp(-(\sigma r)^2)$

boundary nodes which lie in the supporting region/stencil for the node i and $\mathbf{W}_{i,j}^{(x)}$, $\mathbf{W}_{i,j}^{(y)}$, $\mathbf{W}_{i,j}^{(xx)}$ and $\mathbf{W}_{i,j}^{(yy)}$ are the RBF-FD weights corresponding to the differential operator $\partial/\partial x$, $\partial/\partial y$, $\partial^2/\partial x^2$ and $\partial^2/\partial y^2$ respectively. These weights are obtained by solving the system of equation (13) for corresponding differential operators applied to the basis functions.

2.2. Time Splitting

Explicit and implicit discretization schemes are used to approximate time derivatives appearing in equation (3). Description of each approach has been detailed below:

2.2.1. Explicit Approach

Explicit Euler discretization of time derivative appearing in equation (3) can be written as

$$\frac{\vec{V}^{*} - \vec{V}^{n}}{\partial t} = -\left(\vec{V}^{n}.\nabla\right)\vec{V}^{n} + (1/Re)\,\nabla^2\vec{V}^{n} \tag{18}$$

At the end of each time step, continuity condition is satisfied by Poisson equation (6) with non-zero source term. However, intermediate velocity field may not satisfy continuity [21] [22]. RBF-FD approximation of spatial derivatives of equation (18) in 2D Cartesian form can be written as:

$$\frac{u_i^* - u_j^n}{\Delta t} = -u_i^n \sum_{j=1}^{N} \mathbf{W}_{i,j}^{(x)} u_j^n - v_i^n \sum_{j=1}^{N} \mathbf{W}_{i,j}^{(y)} u_j^n + \frac{1}{Re} \sum_{j=1}^{N} \left(\mathbf{W}_{i,j}^{(xx)} + \mathbf{W}_{i,j}^{(yy)} \right) u_j^n \tag{19}$$

$$\frac{v_i^* - v_j^n}{\Delta t} = -u_i^n \sum_{j=1}^{N} \mathbf{W}_{i,j}^{(x)} v_j^n - v_i^n \sum_{j=1}^{N} \mathbf{W}_{i,j}^{(y)} v_j^n + \frac{1}{Re} \sum_{j=1}^{N} \left(\mathbf{W}_{i,j}^{(xx)} + \mathbf{W}_{i,j}^{(yy)} \right) v_j^n \tag{20}$$

Intermediate velocity components can be determined from values of previous iteration using equations (19) and (20). Then the pressure values P^{n+1} can be calculated by solving Poisson equation (15) using intermediate velocity values. Velocity values for next iteration can then be calculated using equations (16) and (17).

Although explicit methods are known to be computationally efficient and are low on memory consumption, strict stability requirements put by CFL conditions ($\Delta t < C\Delta x / v_{max}$, where Δt is time step, Δx is space step, C is a constant and v_{max} is maximum particle velocity) severely limit their application. Moreover, the Euler explicit scheme is only first order accurate. Therefore, accuracy of the solution is compromised, especially at regions of high gradients, unless very high nodal density is introduced. The higher nodal density calls for smaller time steps to meet CFL criterion which slows the time step marching.

2.2.2. *Implicit Approach*

The following approach has been used to achieve second-order accurate implicit in time scheme for velocity momentum equation (3):

1. Second order explicit Adams-Bashforth scheme is used for convective term appearing in equation (3), and
2. second order implicit Crank-Nicolson scheme is used for viscous term appearing in equation (3).

Both the schemes are second order accurate which helps reduce time discretization error of the overall equation. Although Adams-Bahsforth scheme is explicit in time and is somehow affected by CFL stability conditions; the restrictions are more relaxed than for Euler Explicit scheme [23]. Moreover, numerical viscous stability restrictions are eliminated due to implicit treatment of viscous term [24]. Therefore, larger time steps values can be chosen to enable faster marching in time. Discretized forms of convective and viscous terms are shown below:

$$\left(\vec{V}^n.\nabla\right)\vec{V}^n = \frac{1}{2}\left[3\left(\vec{V}^n.\nabla\right)\vec{V}^n - \left(\vec{V}^{n-1}.\nabla\right)\vec{V}^{n-1}\right] \tag{21}$$

$$\frac{1}{Re}\nabla^2\vec{V}^n = \frac{1}{2Re}\left[\nabla^2\left(\vec{V}^n + \vec{V}^*\right)\right] \tag{22}$$

Hence equation (3) can be expressed as:

$$\begin{aligned}\frac{\vec{V}^* - \vec{V}^n}{\Delta t} = &-\frac{1}{2}\left[3\left(\vec{V}^n.\nabla\right)\vec{V}^n - \left(\vec{V}^{n-1}.\nabla\right)\vec{V}^{n-1}\right] \\ &+\frac{1}{2Re}\left[\nabla^2\left(\vec{V}^n + \vec{V}^*\right)\right]\end{aligned} \tag{23}$$

RBF-FD approximation of the 2-D spatial derivatives appearing in equation (23) is as follow:

$$
\begin{aligned}
u_i^* - \frac{\Delta t}{2Re} \sum_{j=1}^{N} \left(\mathbf{W}_{i,j}^{(xx)} + \mathbf{W}_{i,j}^{(yy)} \right) u_j^* = u_i^n + \\
\Delta t \Bigg[-\frac{1}{2} \Bigg\{ 3 \Bigg(u_i^n \sum_{j=1}^{N} \mathbf{W}_{i,j}^{(x)} u_j^n + v_i^n \sum_{j=1}^{N} \mathbf{W}_{i,j}^{(y)} u_j^n \Bigg) \\
- \Bigg(u_i^{n-1} \sum_{j=1}^{N} \mathbf{W}_{i,j}^{(x)} u_j^{n-1} + v_i^{n-1} \sum_{j=1}^{N} \mathbf{W}_{i,j}^{(y)} u_j^{n-1} \Bigg) \Bigg\} \\
+ \frac{1}{2Re} \sum_{j=1}^{N} \left(\mathbf{W}_{i,j}^{(xx)} + \mathbf{W}_{i,j}^{(yy)} \right) u_j^n \Bigg]
\end{aligned}
\tag{24}
$$

$$
\begin{aligned}
v_i^* - \frac{\Delta t}{2Re} \sum_{j=1}^{N} \left(\mathbf{W}_{i,j}^{(xx)} + \mathbf{W}_{i,j}^{(yy)} \right) v_j^* = v_i^n + \\
\Delta t \Bigg[-\frac{1}{2} \Bigg\{ 3 \Bigg(u_i^n \sum_{j=1}^{N} \mathbf{W}_{i,j}^{(x)} v_j^n + v_i^n \sum_{j=1}^{N} \mathbf{W}_{i,j}^{(y)} v_j^n \Bigg) \\
- \Bigg(u_i^{n-1} \sum_{j=1}^{N} \mathbf{W}_{i,j}^{(x)} v_j^{n-1} + v_i^{n-1} \sum_{j=1}^{N} \mathbf{W}_{i,j}^{(y)} v_j^{n-1} \Bigg) \Bigg\} \\
+ \frac{1}{2Re} \sum_{j=1}^{N} \left(\mathbf{W}_{i,j}^{(xx)} + \mathbf{W}_{i,j}^{(yy)} \right) v_j^n \Bigg]
\end{aligned}
\tag{25}
$$

Equation (24) can be written in more concise form as:

$$[A]\{u^*\} = [B]\{u^n\} + [C]\{u^{n-1}\} \tag{26}$$

where

$$A_{i,j} = \begin{cases} 1 - \Delta t/2\,(\mathbf{visc}_{i,j}) & (i = j) \\ -\Delta t/2\,(\mathbf{visc}_{i,j}) & (i \neq j) \end{cases}$$

$$B_{i,j} = \begin{cases} 1 + \Delta t/2 \left(-3\mathbf{conv}^n_{i,j} + \mathbf{visc}_{i,j} \right) & (i = j) \\ \Delta t/2 \left(-3\mathbf{conv}^n_{i,j} + \mathbf{visc}_{i,j} \right) & (i \neq j) \end{cases}$$

$$C_{i,j} = \Delta t/2 \left(\mathbf{conv}^{n-1}_{i,j} \right)$$

$$\mathbf{conv}^n_{i,j} = u^n_i \mathbf{W}^{(x)}_{i,j} + v^n_i \mathbf{W}^{(y)}_{i,j}$$

$$\mathbf{conv}^{n-1}_{i,j} = u^{n-1}_i \mathbf{W}^{(x)}_{i,j} + v^{n-1}_i \mathbf{W}^{(y)}_{i,j}$$

$$\mathbf{visc}_{i,j} = 1/Re \left(\mathbf{W}^{(xx)}_{i,j} + \mathbf{W}^{(yy)}_{i,j} \right)$$

Matrix equations can similarly be formulated for v^* as:

$$[A]\{v^*\} = [B]\{v^n\} + [C]\{v^{n-1}\} \tag{27}$$

Intermediate velocity components are therefore, calculated by solution of matrix equations (26) and (27). Subsequently, equations (15) to (17) are used to calculate pressure and velocity values for next iteration. The process requires simultaneous solution of matrix equations which is computationally expensive. However due to *local* feature of RBF-FD, sparse coefficient matrices are generated which make the solution process fast and are low on memory. The larger time steps allowed by the implicit treatment make the convergence process faster for fixed number of iterations in steady state problems. Therefore, overall computational efficiency improves for Implicit RBF-FD.

3. Solution Algorithm

After representing the domain with finite number of particles (or nodes) and applying initial conditions, the following numerical procedure is used:

1. Intermediate velocities values ($\vec{V}^*$) are calculated at each node for the particular time step. For Euler explicit approach, equations (19) and

(20) are used. For implicit approach, system of equations formed by evaluating equations (26) and (27) at each node is solved to obtain ($\vec{V}^*$). The boundary conditions for intermediate velocity are taken to be the same as nodal velocities at next time iteration on the boundary.

2. Equation (15) is solved using known values of intermediate velocities ($\vec{V}^*$) at the time step to find the values of pressure at each node. The Pressure values on the boundaries are obtained using the equation $n.\nabla P_b^{n+1} = (1/\Delta t)|\vec{V}^* - \vec{V}^{n+1}|_b$, where n is the unit vector in outward normal direction to the boundary and subscript b represents the values at the boundary.
3. Finally, equations (16) and (17) are used to update the velocity components for next time step.
4. Convergence is monitored by calculating the norm of difference in velocity vectors between two consecutive time steps. The process (Step 1-3) is repeated until desired convergence is achieved.

As RBF-FD generates a sparse matrix, Generalized Minimum Residual (GMRES) method with incomplete LU decomposition for preconditioning [25] is used for solution of matrix equations (15), (26) and (27). The sparse matrix equation greatly reduces the computational load and memory requirement of the program

4. Adaptive Shape Parameter (ASP) for Radial Basis Function

It has been discussed before that choice of good value of shape parameter (σ) significantly affects the accuracy of RBF interpolation. Wang [26] states the sensitivity of results with choice of shape parameter as one of the biggest limitations of RBF. Huang et al [15] mentioned that accuracy of the solution can be improved by making the basis function flatter. For example in RBF-IMQ, the basis function can be made flatter by increasing the value of . However, flattening the basis function increases the condition number of the coefficient matrix of RBF weights (as in Equation (13)) making the problem ill-conditioned. Kansa [16] found that condition number of coefficient matrix was a key factor in determining the accuracy of the RBF interpolation. Therefore, the choice of shape parameter value has to be a balance between accuracy related to flatter basis function and round off error arising from ill-conditioning of coefficient matrix appearing in equation (13). Rippa [13] mentioned that choice of a good value of shape parameter should take into account the number and distribution of data points in support domain, the basis function and condition number of the coefficient matrix.

During flow simulations, nodal distribution within the domain is varied to achieve optimal nodal density. Moreover, use of randomly distributed nodes is necessitated in many cases. In such situations, each data point will have different node distribution patterns within its influence domain. Therefore, use of a globally similar value shape parameter, for all the particles within the entire domain, will adversely affect the well conditioning of the coefficient matrix. Figure 2 outlines the trend of condition number of coefficient matrix with varying value of shape parameter (σ) for various RBFs. The plots are obtained on 41x41 pseudo random grid where node locations are disturbed slightly from their corresponding uniform grid positions. It can be observed that, irrespective of the basis function used, the range of shape parameter, corresponding to lower condition numbers of coefficient matrix, varies with the nodal spacing. Hence the accuracy of the solution would vary by changing the number and distribution of nodes for a constant shape parameter. For such domains, if fixed values are used, the round off errors caused by ill-conditioning sometimes dominates and the matrix solution becomes unstable hence causing breakdown of the solution process [17]. This puts severe limitations on the use of non-uniform or random particle distribution within the domain. Therefore, for the problems where same RBF function is used for the entire domain, choosing shape parameter value based on number and distribution of neighbouring data points could keep the condition number of coefficient matrix to the minimum.

The choice of the good value of shape parameter is still a hot topic in research and various authors have suggested different methods of finding an optimum shape value for different problems [11], [13], [26], [15], [17]. However, for present study, a commonly used scheme, presented by Franke [11], has been used which suggests the shape parameter as $\sigma_i = 1.25D/\sqrt{N}$ (Where N is the number of data points in the influence domain of the particle i and D is the diameter of the minimal circle enclosing all the data point). Other schemes for calculating optimum shape parameters can also be tested to further validate the concept.

For the adaptive shape parameter concept, value of (σ) is calculated exclusively for each data point and its value is decided based on number and distribution of neighbouring particles in the influence domain. Besides ensuring accuracy and well-conditioned coefficient matrix, use of adaptive shape parameter also allows larger variation of nodal density within the domain.

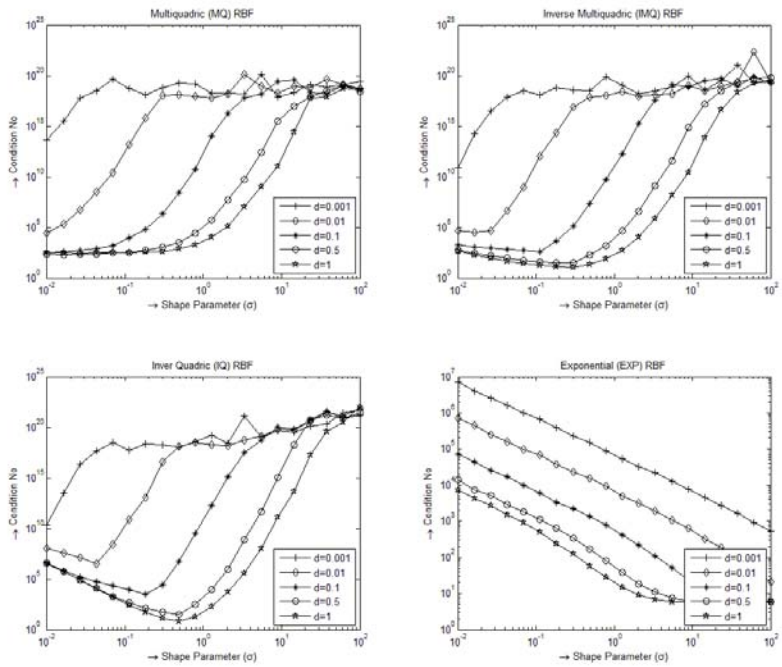

Figure 2: Variation of condition number of coefficient matrix with shape parameter

5. Numerical Tests

5.1. Test of Accuracy

Accuracy tests have been conducted for Implicit RBF-FD method to establish spatial and temporal order of accuracy. For this purpose, decaying vortex problem has been selected. The problem has a known analytical solution and is often used to verify the accuracy of new methods [24], [27], [28], [29]. Theoretical solutions for velocity and pressure fields are:

$$u(x,y,t) = -cos(\pi x)sin(\pi y)exp(-2\pi^2 t/Re) \tag{28}$$

$$v(x,y,t) = sin(\pi x)cos(\pi y)exp(-2\pi^2 t/Re) \tag{29}$$

$$p(x,y,t) = -0.25\left((2\pi x) + sin(2\pi y)\right)exp(-4\pi^2 t/Re) \tag{30}$$

The flow Reynolds number is defined as $Re = \rho UL/\mu$, where ρ is the fluid density, U is maximum initial flow velocity, L is the length of vortex and μ is the dynamic viscosity. Numerical solution of the problem has been obtained over a square domain which spans $[-0.5, 0.5]\times[-0.5, 0.5]$. The domain is represented by uniform as well as pseudo random nodal arrangement. Randomness has been applied by introducing perturbation in the original (uniform grid) location of the nodes. This Random perturbation is however restricted to 20% of the grid spacing to avoid excessive clustering of nodes. The initial conditions have been defined by using analytical solutions of velocity and pressure (equations (28) - (30)) on respective nodal coordinates at $t = 0$. Dirichlet boundary conditions have also been defined at all the four boundaries using theoretical expressions for velocity and pressure at time instant t.

In order to evaluate the order of accuracy in space, numerical solutions are obtained at $t = 0.4$ sec for different values of nodal spacing. Flow Reynolds number has been set as 10 and time step has been chosen to be 10^{-4} sec. The total error for each case has been calculated by evaluating norm-2 of the difference between numerical and analytical velocity and pressures values at all the nodes. Order of accuracy has been calculated as slope of total error and grid spacing (h) on a logarithmic scale. The results for pressure and velocity have been shown in Table 2. Results for v-component of velocity have not been shown because these are similar to those of u-component of velocity. On a uniform grid, velocity is found to be third order accurate in space. However, the order of accuracy reduces on random grid. The order of accuracy for pressure is around 2.85 and it does not change significantly with randomness of nodes. The order of accuracy in time has been calculated by simulating the problem at various time steps on a 51×51 uniform grid. The method is found to be first order accurate in time for both velocity and pressure which is consistent with the observation of previous researches [30], [31]. Order of accuracy in time can be improved further by incorporating strict divergence constraints on intermediate velocity field as suggested by Brown et al [30]. Moreover, introducing incremental pressure correction in fractional step schemes, such as suggested by Goda [20], is shown to have improved order of accuracy in time [31].

5.2. Lid Driven Cavity Flow Problem

The proposed schemes have been validated by solving Lid Driven Cavity Flow problem at various Reynolds Numbers and comparing the results with benchmark solutions provided by Ghia et al [18]. Applicability of schemes

Table 2: Order of accuracy in space for Implicit RBF-FD

Grid Size (h)	$\|error\|_2$	
	Uniform Grid	Random Grid
u-component of velocity		
0.05	4.44E-4	2.82E-4
0.04	2.93E-4	1.74E-4
0.025	9.09E-5	5.90E-5
0.02	4.56E-5	3.48E-5
0.01	3.53E-6	3.51E-6
Order of Accuracy	3.16	2.67
Pressure		
0.05	3.56E-4	3.40E-4
0.04	2.19E-4	2.41E-4
0.025	5.80E-5	6.60E-5
0.02	2.72E-5	3.76E-5
0.01	3.53E-6	4.57E-6
Order of Accuracy	2.86	2.85

has been verified on uniform, non-uniform and random grids. For uniform grid, the nodal spacing has been kept constant throughout the domain. For non-uniform grid, nodal spacing has been varied in a controlled manner in order to keep a higher the nodal density at regions where large gradients of field variables are expected. This has been done to optimize the computational effort so as to achieve greater accuracy with less number of nodes. Random grid represents the domain where nodes have been distributed randomly. The random distribution of nodes has been achieved by incorporating Sobol Sequence in coordinate location of the nodes. Low discrepancy Sobol Sequence randomizes the nodal spacing while still maintaining an overall uniformity in distribution of nodes. Three different types of grids used for the study have been shown in figures 3(a) - 3(c).

The velocity boundary conditions are directly obtained from physical constraints. On all the four walls, velocity component normal to boundary is zero. This ensures that there is no penetration of flow across the boundary. Moreover, no-slip boundary conditions dictate that tangential component of velocity of flow along the boundary τ remains constant and equal to the speed of the boundary itself. So, $(\vec{u}_n) = 0$ and $(\vec{u}_t) = C_2$ at boundary τ where, $(\vec{u}_n)$ and $(\vec{u}_t)$ are the velocity components in outward normal and tangent direction of boundary respectively and C_2 is a constant. Neumann Pressure boundary conditions are introduced using the procedure mentioned in Section 3. Implementation of Neumann boundary condition for pressure has been achieved through locally orthogonal grid near the boundary. For uniform and non-uniform particle distribution, condition of locally orthogonal grid is naturally satisfied. However, for random particle distribution,

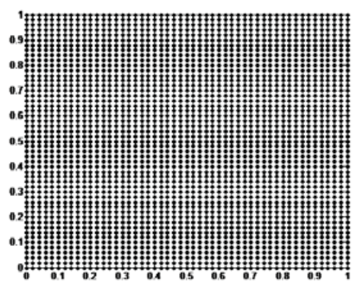

(a) Uniform distribution

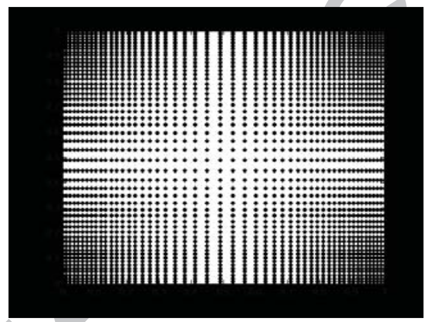

(b) Non-uniform distribution

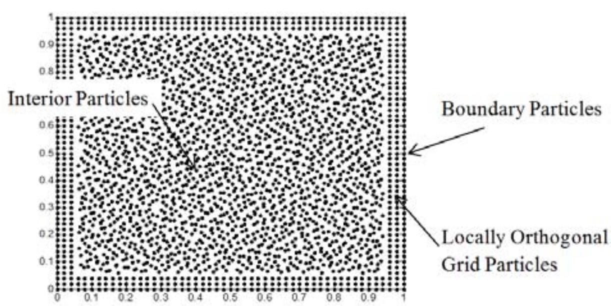

(c) Random Distribution (for interior nodes)

Figure 3: Various configurations of particle distribution

Table 3: Required grid sizes for each test case (Lid driven cavity flow)

Reynolds number	Required grid size	
	Explicit RBF-FD	Implicit RBF-FD
100	91×91	71×71
400	121×121	71×71
1000	151×151	101×101

inner particles may not remain orthogonal to the boundary. Therefore, special care has to be taken to ensure locally orthogonal grid near the boundary. Implementation of locally orthogonal grid for random nodal distribution has been shown in figure 3(c).

5.2.1. Comparison of Implicit and Explicit RBF-FD Schemes

The results for Lid Driven cavity flow have been calculated at Reynolds number 100, 400 and 1000, respectively. For Explicit RBF-FD approach, the time step has been kept at 5×10^{-4} whereas for implicit approach, a time step of 10^{-3} has been chosen. Grid configuration has been kept similar for all the cases to ensure a valid comparison. Non-uniform grid, with nodal spacing ratio of 2.5 between corner-to-centre nodes, has been used for all the cases. Constant values of shape parameters have been used here. Resultant velocity plots, at all three Reynolds numbers, obtained from explicit RBF-FD solution are shown in figure 4(a) - 4(c). Similar plots for implicit RBF-FD approach are shown in figure 5(a) - 5(c). Table 3 shows the optimum grid sizes required to get accurate results for each case.

It can be observed that for implicit solutions, required accuracy can be achieved with relatively coarser grid compared to the explicit solution. This is due to higher order of accuracy achieved during time splitting of governing equations which suffer from less discretization error. Moreover, implicit treatment also eliminates the numerical viscous stability restrictions. These restrictions are particularly sever at low Reynolds numbers and near the boundaries [28]. Therefore, implicit schemes work well even for larger time step values. Significant improvement in CPU time was observed during numerical tests while using implicit scheme. For example, at Re 100 using 91×91 grid, the CPU time for implicit the scheme was 7114 sec, whereas for explicit scheme, it was 36306 sec using Intel ® 3.1 GHz Processor machine. Thus, the computation time was reduced by a factor of 5 using implicit scheme. Possibility of using larger time step and higher accuracy at relatively coarser grids makes the implicit RBF-FD computationally more efficient and stable technique for solution of Navier-Strokes equations in primitive variable form.

5.2.2. Effect of Nodal Distribution

In order to study the effect of changing nodal distribution with the domain, a comparison of results from uniform and non-uniform grids has been presented. The test cases have been run at Reynolds Numbers 100 and 400 on 71×71 grids using implicit approach. The results obtained on both uniform and non-uniform grids have been plotted together in figure 6. It can be observed that non-uniform grid was able to capture the velocity gradients more accurately due to higher nodal density at critical areas. Therefore, selectively distributing the particles in the domain to achieve the nodal density according to expected flow characteristics and gradient of field variables;

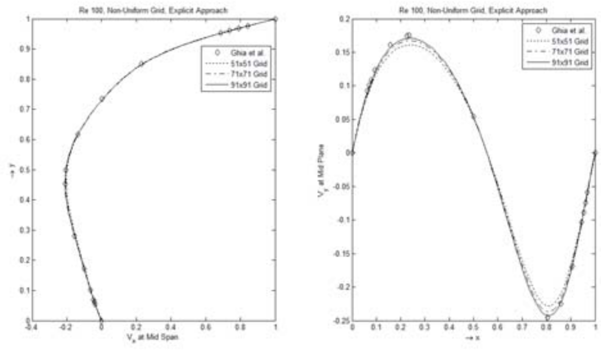

(a) Re 100

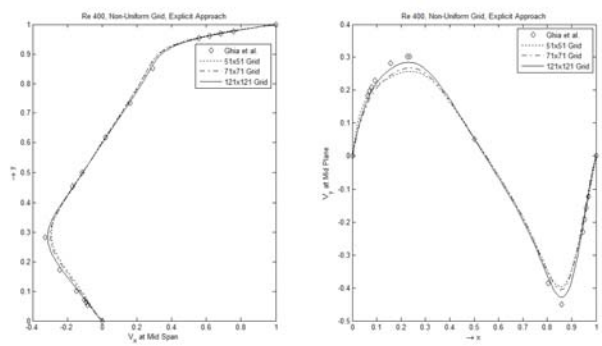

(b) Re 400

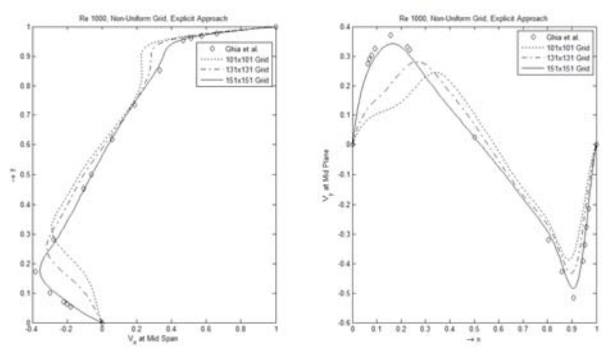

(c) Re 1000

Figure 4: Results for explicit approach

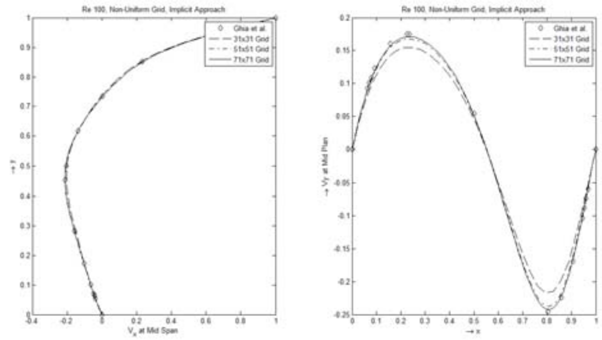

(a) Re 100

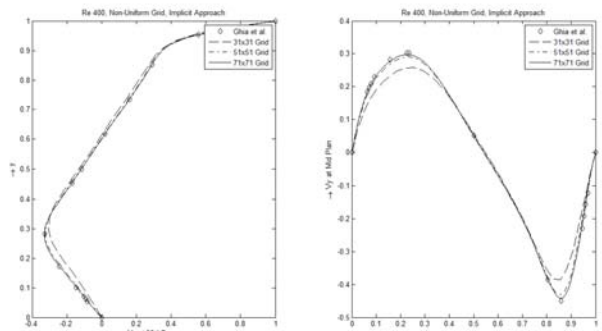

(b) Re 400

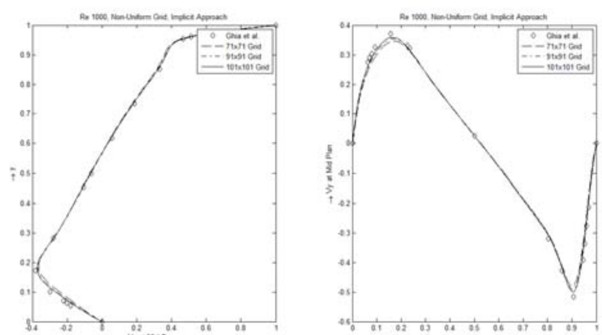

(c) Re 1000

Figure 5: Results for implicit approach

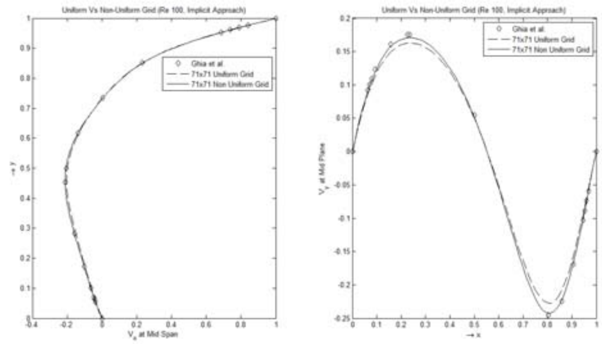

(a) Re 100

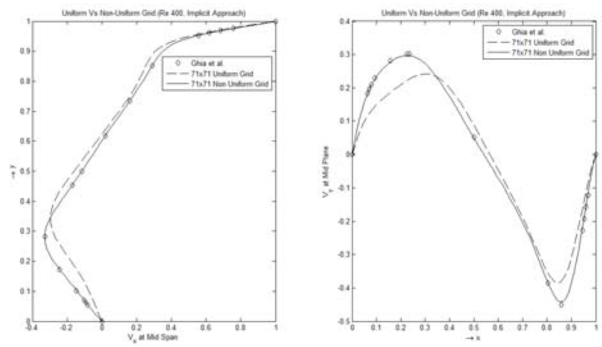

(b) Re 400

Figure 6: Comparison of Results on uniform and non-uniform grids

helps achieve accurate results even for less number of nodes.

Meshless particle methods often employ random particle distribution. Therefore, implicit scheme has been used to solve the flow case over random particle distribution at Re 100. Grid size of 51×51 was chosen and results were compared with benchmark results provided by Ghia et al [18]. Resultant velocity profiles in Figure 7, show good agreement with benchmark solution which validates the application of suggested scheme on random grid.

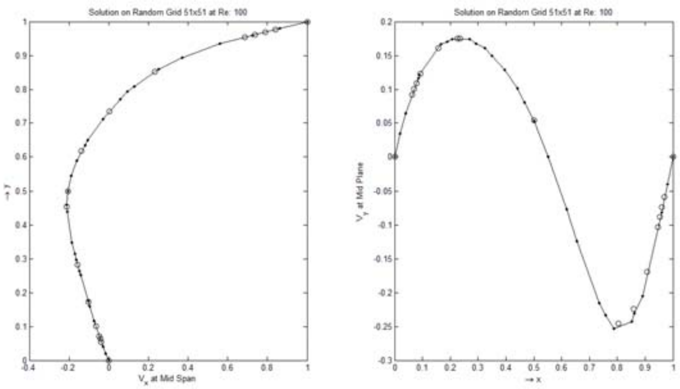

Figure 7: Results on random grid

5.2.3. Comparison of Constant and Adaptive Shape Parameters

It can be observed from figures 3(b) and 3(c) that the nodal spacing, and thus the distribution of nodes, varies considerably within the domain. Therefore, the condition number of coefficient matrix can go higher for certain data points thus affecting the accuracy of solution. In order to avoid the possible ill-conditioning of coefficient matrix, shape parameter value can be made adaptive with nodal distribution. For this purpose, the value of shape parameter is chosen separately at each node depending upon the particular nodal distribution in the influence domain. This ensures that the problem remains well posed at all data point.

The results of lid driven cavity flow problem at Re 400 and 1000 with fixed and adaptive shape parameter using implicit RBF-FD technique have been compared. Non-uniform grid size of 51×51 is used at Re 400 whereas 101×101 sized grid is used for Re 1000. For non-uniform grid, if a constant value of shape parameter (σ) is used, the ratio of nodal spacing between corner-to-centre nodes is limited to 2.5. Any value higher than 2.5 will cause

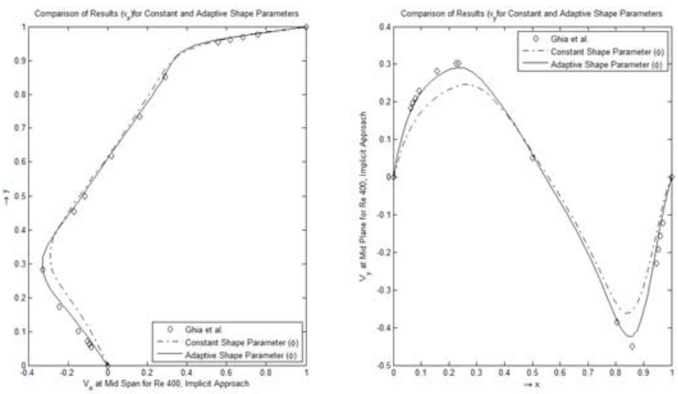

Figure 8: Results for fixed and adaptive RBF shape parameter (σ): *Re* 400 over 40×40 grid

ill-conditioning (as discussed before) and solution will break down without reaching convergence. However, when adaptive shape parameter technique is used, the ratio of nodal spacing between corner-to-centre nodes can be increased up to 4.0 without introducing ill-conditioning. The grid can therefore be made much more refined close to the walls than for fixed shape parameter approach. The results are therefore, more accurate for same number of nodes within the domain. The velocity plots at *Re* 400 and 1000 are shown in figures 8 and 9, respectively (for fixed and adaptive RBF shape parameters). Significant improvement in results is observed with the use of adaptive shape parameters.

5.3. Flow past Circular Cylinder

In this work, implicit RBF-FD method with adaptive shape parameter has been used to simulate laminar flow over a circular cylinder. The flow problem has extensively been studied by previous researchers [32], [33], [34], [35],

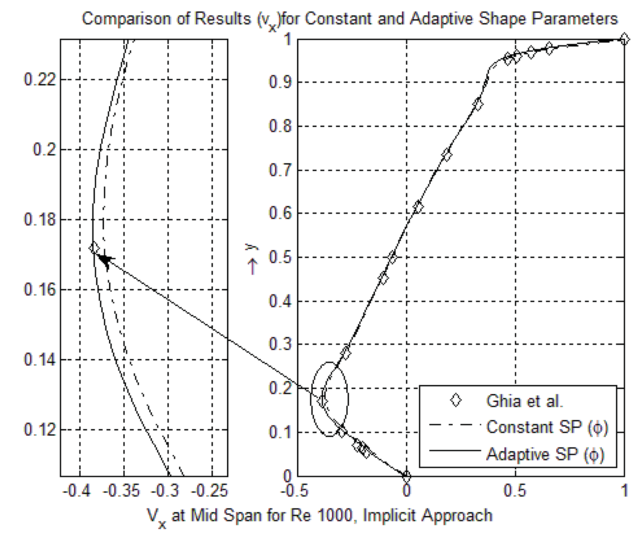

(a) vx

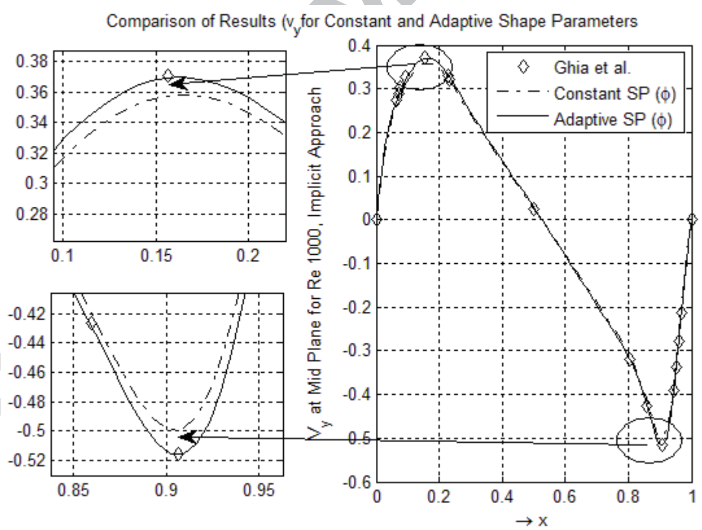

(b) vy

Figure 9: Results for fixed and adaptive RBF shape parameter(σ): *Re* 1000 over 40×40 grid

[36], [37], [38] and is often used as benchmark problem to examine the performance of new numerical techniques. Flow around cylinder demonstrates a periodically unsteady pattern when its Reynolds number $Re = (U_\infty D)/\nu$ is larger than the critical value ($Re \approx 49$) [9], where U_∞ is the free stream velocity, D is the diameter of cylinder and ν is the kinematic viscosity. For low Reynolds numbers ($Re < 50$), steady flow field is obtained around cylinder. However at moderate range of Reynolds numbers ($50 < Re < 190$), the flow remains laminar but a vortex shedding phenomenon (also known as Karman Vortex Street) is observed. In the present work, flow around circular cylinder has been solved at Re 10, 20, 40, 100 and 200 to simulate both steady and unsteady flow patterns. Configuration of domain geometry is shown in figure 10. Total length of the rectangular domain is kept 30 times the diameter of the cylinder. Inlet is placed 5 times the diameter away from the centre of cylinder. Top and bottom boundaries are located at a transversal distance of 6 times the cylindrical diameter. Free Stream velocity U_∞ has been specified at inlet boundary to correspond to Reynolds number of flow. Boundary conditions at top and bottom boundaries are the same as inflow boundary. No slip boundary conditions are specified at cylinder surface ($u = v = 0$, where u and v are Cartesian components of velocity) and zero velocity gradient condition ($\partial u/\partial x = \partial v/\partial x = 0$) has been applied at outflow boundary. Pressure at outflow boundary has been obtained by the use of equation (23).

The nodal distributions have been shown in figure 11 for steady and unsteady flow cases. For unsteady flow cases, a finer grid is used near the cylinder to accurately capture time varying flow. A total of 16061 and 17758 nodes have been used to represent the domain for steady and unsteady flow

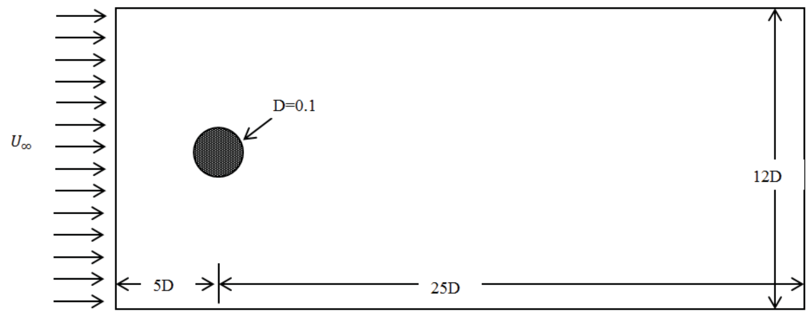

Figure 10: Geometric configuration for flow around Circular Cylinder

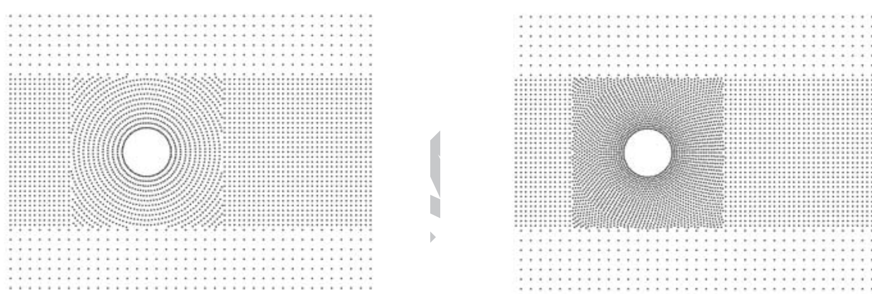

(a) Grid for steady flow cases (b) Grid for un-steady flow cases

Figure 11: Nodal distribution for flow around circular cylinder

cases, respectively. The nodal arrangement is somewhat like a polar mesh close to the cylinder. However in the far field (about 1.5 times the diameter from the centre of cylinder), the nodal arrangement switches to resemble regular Cartesian grid. The particles are closely spaced in the region where wake is expected. However in the far field and outside the expected wake region, density of particle has been reduced. Time step value has been chosen to be 0.005 sec for simulation.

5.3.1. Steady Laminar Flow

Vortex plots for steady flow cases (*Re* 10, 20 and 40) have been illustrated in figure 12(a) - 12(c). In all the three cases, a pair of perfectly aligned vortices forms behind the cylinder which is consistent with the results of previous researchers [32], [33], [34], [35], [38], [39], [40]. The quantitative values of length of recirculating region from rearmost point of the cylinder to the end of the wake (L_{sep}) and drag coefficient (C_D) have been compared with the results obtained during previous studies [32], [33], [34], [35], [38], and placed in Table 4. The flow parameters obtained are in good agreement with the results of previous researchers for the three Reynolds numbers.

5.3.2. Unsteady Laminar Flow

Unsteady behaviour of flow behind the cylinder is studied at *Re* 100 and 200. The resulting vortex pattern for complete oscillation cycle of flow has been shown in figure 13 and 14 for *Re* 100 and 200, respectively. Oscillating flow pattern also affects the drag and lift coefficients (C_L and C_D) with changing time. Profiles of lift and drag coefficients have been shown in figure 15. From these plots, quantitative values of parameters like Strouhal number (St) and mean / peak values of lift and drag coefficients have been evaluated and compared with the results from previous studies [36], [37], [38] in Table 5. The results are in good agreement with previously calculated values. The vortex shedding frequency increases with increase in Reynolds number. Moreover, oscillation profile of flow is followed by similar pattern of variation in lift and drag coefficients. These observations are also in agreement with the results of previous researchers.

Table 4: Comparison of length of recirculating region (L_{sep}) and drag coefficient (C_D) for *Re* 10, 20 and 40

Source	L_{sep}	C_D
Re=10		
Dennis et al. [35]	0.252	2.85
Takami et al. [33]	0.249	2.80
Tuann et al. [32]	0.25	3.18
Fornberg [34]	-	-
Present Study	0.25	2.864
Re=20		
Dennis et al. [35]	0.94	2.05
Takami et al. [33]	0.935	2.01
Tuann et al. [32]	0.90	2.25
Fornberg [34]	0.91	2.00
Present Study	0.90	2.066
Re=40		
Dennis et al. [35]	2.35	1.522
Takami et al. [33]	2.32	1.536
Tuann et al. [32]	2.1	1.675
Fornberg [34]	2.24	1.498
Present Study	2.4	1.598

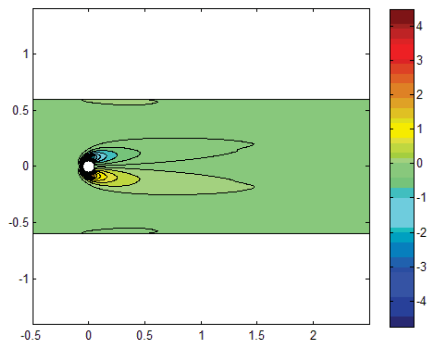

(a) Re=10

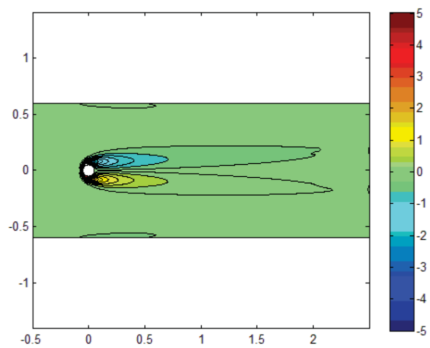

(b) Re=20

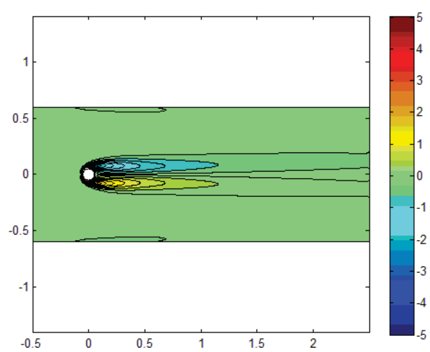

(c) Re=40

Figure 12: Vorticity plots for steady flow at different Reynolds numbers

Table 5: Comparison of Strouhal Number (St), lift and drag coefficients (C_L and C_D) for Re 100 and 200

Source	St	C_D	C_L
Re=100			
Braza et al. [38]	0.160	1.364 ± 0.015	± 0.25
Liu et al. [36]	0.164	1.350 ± 0.012	± 0.34
Belov et al. [37]	-	-	-
Present Study	0.1646	1.344 ± 0.0011	± 0.32
Re=200			
Braza et al. [38]	0.200	1.40 ± 0.05	± 0.75
Liu et al. [36]	0.192	1.31 ± 0.005	± 0.69
Belov et al. [37]	0.193	1.19 ± 0.042	± 0.64
Present Study	0.200	1.3945 ± 0.07	± 0.77

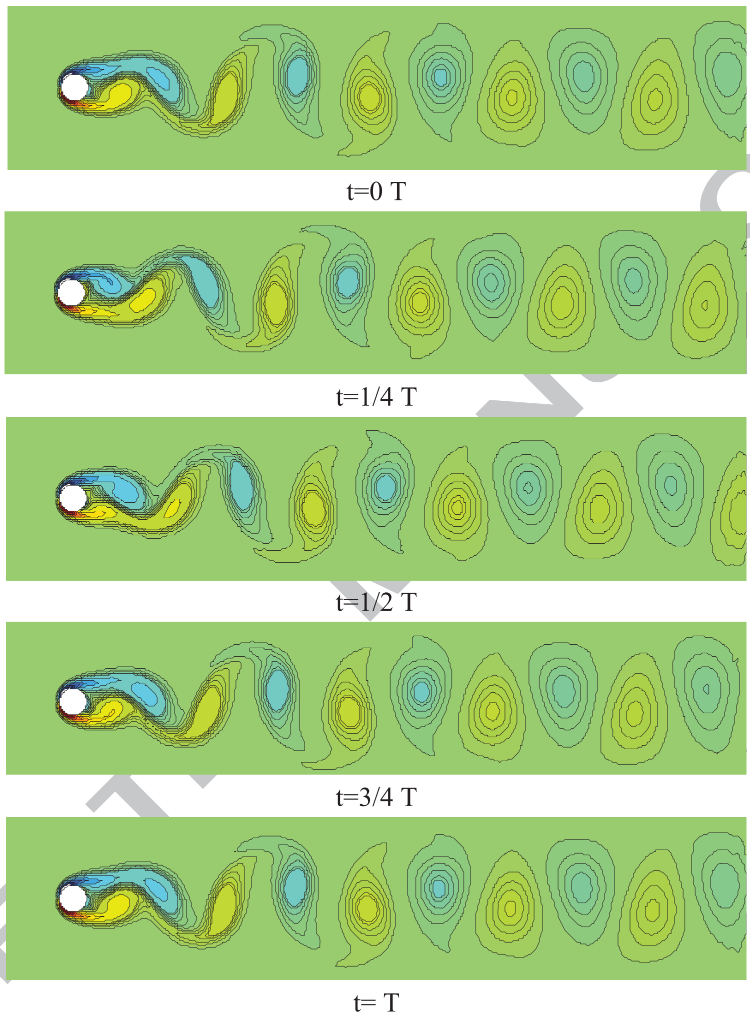

Figure 13: Screenshots of vorticity pattern during oscillatory period (Re 100)

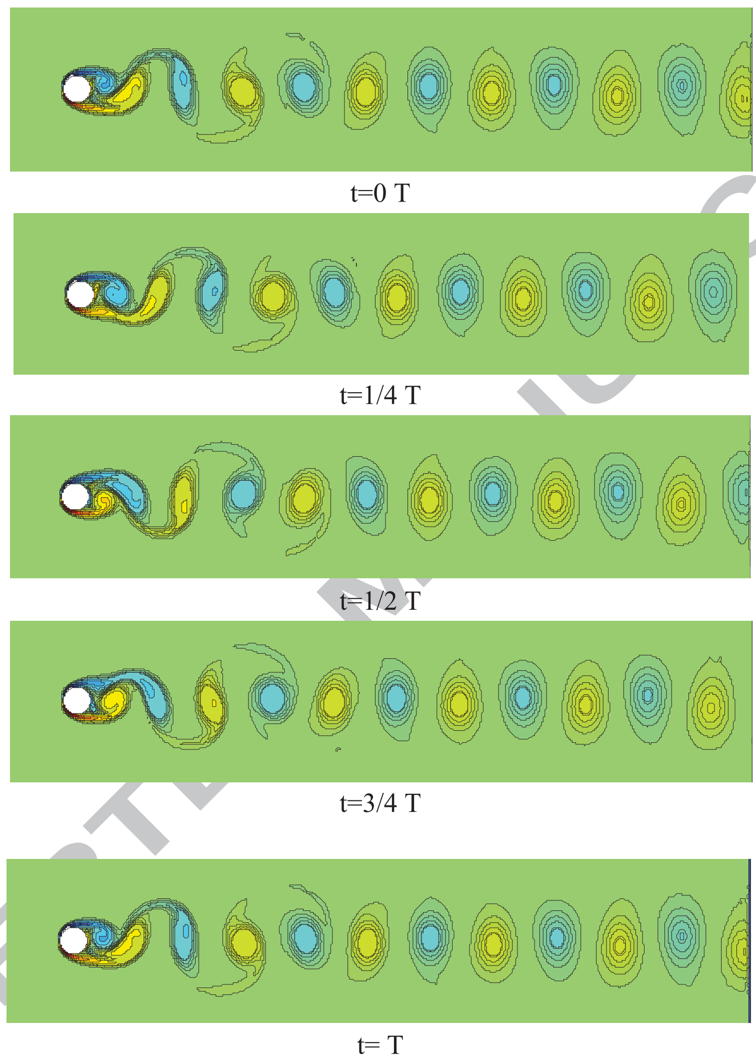

Figure 14: Screenshots of vorticity pattern during oscillatory period (Re 200)

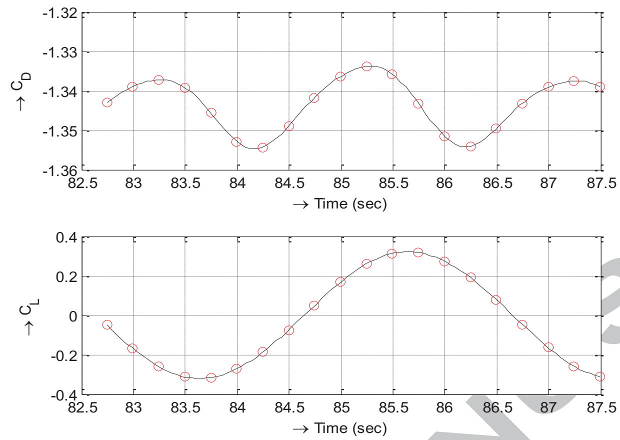

(a) Re=100

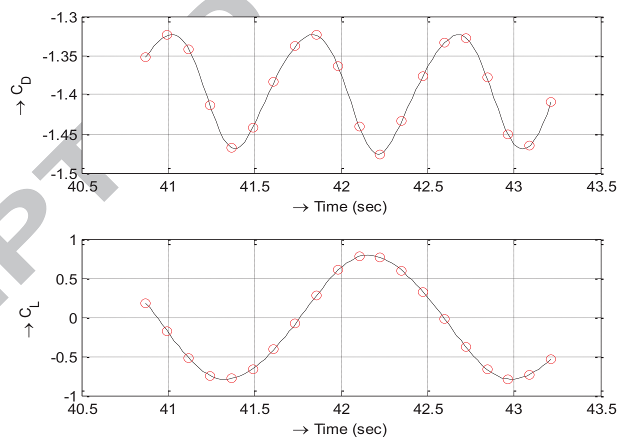

(b) Re=200

Figure 15: Variation of lift and drag coefficients over time for unsteady laminar flow

6. Conclusion

Solution schemes for 2D Navier-Strokes equations in pressure-velocity formulation have been presented using explicit and implicit in time, RBF-FD method. Numerical tests show that both the explicit and implicit methods work fine. However, use of RBF-FD implicit method was found to be more accurate than the RBF-FD explicit method. For explicit method, loss of accuracy was especially prominent at places where larger gradients of flow variables were encountered. Higher accuracy achieved by the use of time-implicit approach produced required accuracy with less number of data points in the domain. Use of non-uniform grid was investigated to capture high gradients of field variable. However, degree of non-uniformity (ratio of largest to smallest nodal displacement) was restricted by resultant ill-conditioning effect on coefficient matrix of RBF-FD weights. Ill-conditioning was also experienced while using finer grid with nodes randomized by Sobol sequence (as it introduces very small nodal displacements at some points). The restrictions were relaxed by the use of adaptive shape parameter (ASP) which ensured good results even for high ratios of nodal displacements. Implicit treatment of N-S equations requires simultaneous solution of matrix equations which is computationally expensive. However, due to use of local RBF-FD scheme, sparse set of matrices are obtained which make the solution process much faster. Moreover, larger time step values allowed by implicit approach as well as less number of data points due to higher order of accuracy contribute towards the efficiency of overall numerical simulation process.

Application of presented scheme may be extended to explore 3D problems. Moreover, other solution schemes can be devised based on different time discretization schemes.

Acknowledgement

The authors acknowledge the valuable comments by the anonymous reviewers which helped improve the research.

References

1. Lucy L. A numerical approach to the testing of fission hypothesis. *Astronomical Journal* 1977;8:1013–1024.

2. B. Nayroles G. Touzot G, Villon P. Generalizing the finite element method: diffuse approximation and diffuse elements. *Computattional Mechanics* 1992;10:307–318.

3. T. Belytschko YL, Gu L. Element free galerkin methods. *International Journal of Numerical Methods in Engineering* 1994;37:229–256.

4. Liu WK, Jun S, Li SF, Adee J, Belytschko T. Reproducing kernel particle methods for structural dynamics. *International Journal for Numerical Methods in Engineering* 1995;38(10):1655–1679.

5. Melenk JM, Babuska I. The partition of unity finite element method: Basic theory and applications. *Computer Methods in Applied Mechanics and Engineering* 1996;139(1-4):289–314.

6. Onate E, Idelsohn S, Zienkiewicz OC, Taylor RL, Sacco C. A stabilized finite point method for analysis of fluid mechanics problems. *Computer Methods in Applied Mechanics and Engineering* 1996;139(1-4):315–346.

7. S. N. Atluri TZ. New meshless local petrovgalerkin approach in computational mechanics. *Computattional Mechanics* 1998;22:117127.

8. Wright GB, Fornberg B. Scattered node compact finite difference-type formulas generated from radial basis functions. *Journal of Computational Physics* 2006;212(1):99–123.

9. Shu C, Ding H, Yeo KS. Local radial basis function-based differential quadrature method and its application to solve two-dimensional incompressible navier-stokes equations. *Computer Methods in Applied Mechanics and Engineering* 2003;192(7-8):941–954.

10. Tolstykh AI, Shirobokov DA. On using radial basis functions in a "finite difference mode" with applications to elasticity problems. *Computational Mechanics* 2003;33(1):68–79.

11. Franke R. Scattered data interpolation: Tests of some method. *Mathematics of Computation* 1982;38(157):181.

12. Hardy RL. Theory and applications of the multiquadric biharmonic method - 20 years of discovery 1968-1988. *Computers and Mathematics with Applications* 1990;19(8-9):163–208.

13. Rippa S. An algorithm for selecting a good value for the parameter c in radial basis function interpolation. *Advances in Computational Mathematics* 1999;11(2-3):193–210.

14. Chinchapatnam PP, Djidjeli K, Nair PB, Tan M. A compact rbf-fd based meshless method for the incompressible navier-stokes equations.

Proceedings of the Institution of Mechanical Engineers Part M-Journal of Engineering for the Maritime Environment 2009;223(M3):275–290.

15. Huang CS, Lee CF, Cheng AHD. Error estimate, optimal shape factor, and high precision computation of multiquadric collocation method. *Engineering Analysis with Boundary Elements* 2007;31(7):614–623.

16. Kansa EJ. Multiquadrics - a scattered data approximation scheme with applications to computational fluid-dynamics .2. solutions to parabolic, hyperbolic and elliptic partial-differential equations. *Computers and Mathematics with Applications* 1990;19(8-9):147–161.

17. Gherlone M, Iurlaro L, Di Sciuva M. A novel algorithm for shape parameter selection in radial basis functions collocation method. *Composite Structures* 2012;94(2):453–461.

18. Ghia U, Ghia KN, Shin CT. High-re solutions for incompressible-flow using the navier stokes equations and a multigrid method. *Journal of Computational Physics* 1982;48(3):387–411.

19. Chorin AJ. Numerical solution of the navier-stokes equations. *Mathematics of computation* 1968;22(104):745–762.

20. Goda K. A multistep technique with implicit difference schemes for calculating two-or three-dimensional cavity flows. *Journal of Computational Physics* 1979;30(1):76–95.

21. Xia J, Leung D. A Stable Numerical Method for the Time Dependent

Navier-Stokes Equations and Its Application in Street Canyon Flows. Springer Berlin Heidelberg; 2003. ISBN 978-3-642-63938-8.

22. Perot J. Comments on the fractional step method. *Journal of Computational Physics* 1995;121(1):190 – 191.

23. Deriaz E. Stability of explicit numerical schemes for smooth convection dominated problems. *bli* 2010;1:0.

24. Kim D, Choi H. A second-order time-accurate finite volume method for unsteady incompressible flow on hybrid unstructured grids. *Journal of Computational Physics* 2000;162(2):411–428.

25. Saad Y, Schultz MH. Gmres: A generalized minimal residual algorithm for solving nonsymmetric linear systems. *SIAM Journal on scientific and statistical computing* 1986;7(3):856–869.

26. Wang JG, Liu GR. On the optimal shape parameters of radial basis functions used for 2-d meshless methods. *Computer Methods in Applied Mechanics and Engineering* 2002;191(23-24):2611–2630.

27. Chew CS, Yeo KS, Shu C. A generalized finite-difference (gfd) ale scheme for incompressible flows around moving solid bodies on hybrid meshfreecartesian grids. *Journal of Computational Physics* 2006;218(2):510–548.

28. Kim J, Moin P. Application of a fractional-step method to incompressible navier-stokes equations. *Journal of Computational Physics* 1985;59(2):308–323.

29. Zang Y, Street RL, Koseff JR. A non-staggered grid, fractional step method for time-dependent incompressible navier-stokes equations in curvilinear coordinates. *Journal of Computational Physics* 1994;114(1):18–33.

30. Brown DL, Cortez R, Minion ML. Accurate projection methods for the incompressible navierstokes equations. *Journal of Computational Physics* 2001;168(2):464–499.

31. Guermond JL, Minev P, Shen J. An overview of projection methods for incompressible flows. *Computer Methods in Applied Mechanics and Engineering* 2006;195(4447):6011–6045.

32. Tuann Sy, Olson MD. Numerical studies of the flow around a circular cylinder by a finite element method. *Computers and Fluids* 1978;6(4):219–240.

33. Takami H, Keller HB. Steady two-dimensional viscous flow of an incompressible fluid past a circular cylinder. *Physics of Fluids* 1969;12(12):II–51–II–56.

34. Fornberg B. A numerical study of steady viscous-flow past a circular-cylinder. *Journal of Fluid Mechanics* 1980;98(Jun):819–855.

35. Dennis S, Chang GZ. Numerical solutions for steady flow past a circular cylinder at reynolds numbers up to 100. *J Fluid Mech* 1970;42(3):471–489.

36. Liu C, Zheng X, Sung C. Preconditioned multigrid methods for unsteady

incompressible flows. *Journal of Computational Physics* 1998;139(1):35–57.

37. Belov A, Martinelli L, Jameson A. A new implicit algorithm with multigrid for unsteady incompressible flow calculations. *AIAA paper* 1995;95:0049.

38. Braza M, Chassaing P, Minh HH. Numerical study and physical analysis of the pressure and velocity-fields in the near wake of a circular-cylinder. *Journal of Fluid Mechanics* 1986;165:79–130.

39. Sen S, Mittal S, Biswas G. Steady separated flow past a circular cylinder at low reynolds numbers. *Journal of Fluid Mechanics* 2009;620:89–119.

40. Firoozjaee AR, Afshar MH. Steady-state solution of incompressible navierstokes equations using discrete least-squares meshless method. *International Journal for Numerical Methods in Fluids* 2011;67(3):369–382.

Highlights

1. A new section has been included for Accuracy test analysis.
2. Point about using accurate time discretization schemes has been included.
3. Correction has been made in iteration number of pressure term. Pressure is computed an n+1 and not at n iteration.
4. Description of boundary conditions has been included in more detail.